PHYSICAL REVIEW B VOLUME 6, NUMBER 5 1 SEPTEMBER 1972

Theoretical Survey of the Sidebands of Sm^{2+} Fluorescence in BaF_2

J. P. Hurrell
Department of Materials Science, University of Southern California, Los Angeles, California* 90007

and

Z. Kam and E. Cohen
Physics Department,† Technion-Israel Institute of Technology, Haifa, Israel
(Received 24 November 1971)

We have investigated the one-phonon sidebands of the fluorescence of divalent samarium in barium fluoride. Transitions from $^5D_0$ to the three multiplets $^7F_0$, $^7F_1$, and $^7F_2$ have been calculated in the crystal-field approximation. Fair agreement is found not only for their frequency dependence, but also for their absolute intensities, which are compared to the intensity of the magnetic-dipole $^5D_0 \rightarrow {}^7F_1$ zero-phonon transition. A sum rule is developed which uniquely specifies all the angular properties of the transitions in terms of one parameter for every contributing multipole. Estimates of the amplitudes of these contributions lie within a factor of 3 of the experimental values. However, significant deviations remain which are attributed to the effects of electron delocalization.

I. INTRODUCTION

Strong fluorescence within the $4f$ shell of rare-earth ions in crystals occurs for sites lacking inversion symmetry; this property is utilized in many solid-state lasers. When, however, the ions occupy sites possessing inversion symmetry, the fluorescence is dominated by the electric-dipole emission associated with phonon-assisted transitions. In this paper we discuss the spectroscopic details of these single-phonon sidebands. We derive explicit expressions for their shapes and oscillator strengths which we apply to the example of divalent samarium in barium fluoride.

During the last decade a number of rare-earth vibronic spectra have been investigated and interpreted with an electron-phonon Hamiltonian calculated in a crystal-field approximation. This approximation is discussed in a recent survey by Wagner[1] where a comprehensive list of references to previous work can also be found. In the $BaF_2:Sm^{2+}$ system, this simple coupling may be pursued with little interference from nebulous side effects. In particular, it is essential that the impurity should possess localized initial, intermediate, and final electronic states before a crystal field calculated at the impurity site can be used as a basis for the electron-phonon interaction. Divalent samarium possesses initial and final states which can lie in the f^6 configuration while the intermediate states are dominated by the low-lying f^5d configuration which is also reasonably well localized: The proximity of this configuration to the conduction band[2] may cause a partial delocalization. Since, however, the vibronic intensity is dependent upon the overlap between initial and intermediate states, this may not provide too serious a limitation. Second, to test the success of this coupling model, the system of impurity plus lattice should have a known vibrational spectrum. Since these modes also depend upon the coupling to some extent, it is necessary to keep the perturbing influence of the impurity small. This can best be satisfied by finding a host crystal in which the samarium ion would be a good fit, namely, same mass and same force constants. Then the modes of the pure crystal can be used without recourse to a Green's-function calculation except as a final refinement. The fit in BaF_2 is tolerably good with mass Sm/mass Ba = 1.1 and radius Sm/radius Ba = 0.9. Recent calculations[3] have followed some of the systematics of various crystal models with this coupling Hamiltonian, using the samarium fluorescence in alkaline-earth fluorides. We have chosen a severe test for the theory by attempting to analyze vibronic spectra accompanying four different electronic transitions in BaF_2. We have used the simple shell-model analysis of the phonon spectrum of BaF_2 derived from neutron-scattering experiments.[4] We develop both the expansion necessary to calculate the crystal fields produced by the phonons and the required theory for the samarium spectroscopy. We derive a relation to determine uniquely all the angular properties of the spectra which is analogous to but different from the results derived by Judd[5] for rare-earth spectra in liquids. We find that the shell model can provide a good basis for the vibronic calculations though the crystal-field results are found to be less accurate; from a detailed comparison with the observed spectra, certain differences emerge which suggest that the nearest-neighbor contributions should be handled more carefully.

II. THEORY

The theory of the weak electron-lattice coupling which we shall use has been extensively discussed by Wagner.[1] We shall merely summarize the part relevant to the present system and then develop the necessary extension for handling the detailed spectroscopic aspects of the crystal-field interaction.

The zero-order states of the system $|i, n\rangle$ are products of electronic states $|i\rangle$ of the rare-earth ions and lattice states $|n\rangle$ (here characterized by the occupation number of one mode). The electron-phonon coupling Hamiltonian is written as a power series in the lattice displacements:

$$\mathcal{H}_{el} = \sum_{\alpha \vec{q} \xi} e[V(\vec{r}_\alpha \vec{q} \xi) a_{\vec{q}\xi} + V^*(\vec{r}_\alpha \vec{q} \xi) a^\dagger_{\vec{q}\xi}] + \cdots .$$

V represents the potential acting on a $4f$ electron (charge e at $\vec{r}_\alpha$) produced by a lattice mode characterized by wave vector $\vec{q}$ and branch index ξ. We assume that the outer $5s$ and $5p$ samarium electrons take the place of the outer barium electrons in setting up the short-range forces which are assumed to remain unchanged. This potential possesses both diagonal and nondiagonal matrix elements between the $|i\rangle$. The diagonal elements result in a shift in the oscillator mean position in configuration space dependent upon the electronic state under consideration, and the nondiagonal elements, which are more important for our problem, relax the Born-Oppenheimer approximation. Higher-order processes produce further mixing of the states and a stiffening of the modes. Formally we may write the new states of the system in the limit of weak-phonon coupling as $|\{i, n\}\rangle$, where

$$|\{i, n\}\rangle = |i, n\rangle + \sum_{jm}{}' \frac{\langle j, m|\mathcal{H}_{el}|i, n\rangle}{E_i - E_j + \hbar\omega(n-m)} |j, m\rangle$$

and all mode indices have been omitted.

When the impurity site has inversion symmetry, $|i\rangle$ possesses definite parity and electronic transitions within the $4f^6$ configuration do not have electric-dipole character and are comparatively weak. Then the major contribution to the sidebands arises from the odd components of V. In our experiments on Sm^{2+}, the initial and all final states lie in the $4f^6$ configuration, and there is only one observed vibronic which may possess partial magnetic-dipole character—this contribution will be considered separately. We may write the electric-dipole matrix element for polarization $\vec{\epsilon}$ as

$$\langle\{i, n\}|e\textstyle\sum_\alpha \vec{\epsilon}\cdot\vec{r}_\alpha|\{f, m\}\rangle .$$

One further consequence of the cubic symmetry of the samarium site is that the fluorescence is isotropic. This isotropy, however, only appears after a sum over phonon states is performed. Consequently, to demonstrate its more obvious consequences, it is convenient to impose a redundant sum over Cartesian components of the dipole matrix element. Then the power radiated per unit angular-frequency bandwidth by one excited atom into solid angle $d\Omega$ for the Stokes sideband,

$$|\{i, n\}\rangle \rightarrow |\{f, n+1\}\rangle ,$$

seen at low temperatures for which all $n = 0$, is given by

$$\frac{2}{3}\sum_x \sum_{\vec{q}\xi}\left(\frac{\omega'^4}{2\pi c^3}\right)\left|\sum_j{}' \frac{\langle i|e\textstyle\sum_\alpha V(\vec{r}_\alpha\vec{q}\xi)|j\rangle\langle j|e\sum_\alpha x_\alpha|f\rangle}{E_i - E_j - \hbar\omega_{\vec{q}\xi}} + \sum_j{}' \frac{\langle i|e\sum_\alpha x_\alpha|j\rangle\langle j|e\sum_\alpha V(\vec{r}_\alpha\vec{q}\xi)|f\rangle}{E_f - E_j + \hbar\omega_{\vec{q}\xi}}\right|^2 \delta(\omega_{\vec{q}\xi} - \omega)\, d\Omega , \tag{1}$$

with an implied sum over degenerate initial and final states. The radiated frequency ω' equals $\omega_0 - \omega$ where ω_0 and ω are the angular frequencies of the parent transition and contributing phonon, respectively.

A. Evaluation of Matrix Elements

We shall be interested in transitions from the $^5D_0$ state at 14 638 cm^{-1} to various members of the ^7F ground multiplet. The static crystalline field admixture of $|J+4\rangle$ into $|J\rangle$ is 2% assuming a cubic-field interaction of 100 cm^{-1} and a spin-orbit interaction $\lambda\vec{L}\cdot\vec{S}$ with $\lambda = 264$ cm^{-1} (these estimates are based on our observed spectra); this admixture will be neglected. We may write

$$\sum_\alpha V(\vec{r}_\alpha\vec{q}\xi) = \sum_{tp}\left(\frac{\hbar}{2MNr_0^2\omega_{\vec{q}\xi}}\right)^{1/2} A_{tp}(\vec{q}\xi)\mathfrak{D}_p^{(t)} ,$$

with

$$\mathfrak{D}_p^{(t)} = \sum_\alpha\left(\frac{4\pi}{2t+1}\right)^{1/2} r_\alpha^t Y_{tp}(\theta_\alpha\varphi_\alpha) ;$$

r_0 (half the lattice constant) equals 3.1 Å and M is the proton mass. We will leave the calculation of A_{tp} for every phonon till Sec. II B. Then evaluation of the various terms in Eq. (1) involves matrix elements of the form

$$\langle Jm|\mathfrak{D}_s^{(1)}|J''m''\rangle\langle J''m''|\mathfrak{D}_p^{(t)}|J'm'\rangle ,$$

and the problem reduces to be similar to that of the calculation of absorption intensities of rare-earth ions treated by Judd,[5] and the two-photon processes discussed by Axe.[6] We shall impose the mild closure that the energy of a multiplet be independent of $J_z(m)$ rather than throwing the whole excited configuration into one energy. The latter procedure enabled Judd to derive some simple relations between the intensities of different transitions, but

would not be valid for the low-lying f^5d configuration. Nevertheless, this approximation will enable all the angular properties of the vibronic problem to be explicitly obtained. We use the Wigner-Eckart theorem to separate the angular dependences and expand the ensuing product of 3-j symbols.

This result, together with the expansions

$$|i\rangle = \sum a^i_m |Jm\rangle\,, \quad |f\rangle = \sum a^f_{m'} |J'm'\rangle\,,$$

with a^i_m, $a^f_{m'}$ determined by the site symmetry, enables Eq. (1) to assume the form

$$\tfrac{2}{3}\sum_{\vec{s}\vec{q}\xi}\left(\frac{e^2\omega'^4}{2\pi c^3}\right)\left(\frac{e^2\hbar}{2MNr_0^2\omega_{\vec{q}\xi}}\right)\Big|\sum_{\substack{mm'\\ tp\lambda}} a^{i*}_m a^f_{m'} A_{tp}\langle Jm|\,T^{(\lambda)}_{p+s}\,|J'm'\rangle\Big|^2 \delta(\omega_{\vec{q}\xi}-\omega)\,d\Omega\,, \tag{2}$$

where

$$\langle Jm|\,T^{(\lambda)}_{p+s}\,|J'm'\rangle = (-1)^{J-m}\begin{pmatrix} J & \lambda & J' \\ -m & p+s & m'\end{pmatrix}\langle J\|\,\tau^{(\lambda)}\,\|J'\rangle$$

and

$$\langle J\|\,\tau^{(\lambda)}\,\|J'\rangle = (-1)^{J+J'+p+s}(2\lambda+1)\begin{pmatrix}1 & \lambda & t\\ s & -p-s & p\end{pmatrix}\sum_{j,J''}\left(\frac{\begin{Bmatrix}1 & t & \lambda\\ J' & J & J''\end{Bmatrix}\langle iJ\|\,\mathfrak{D}^{(1)}\,\|jJ''\rangle\langle jJ''\|\,\mathfrak{D}^{(t)}\,\|fJ'\rangle}{E_{J'}-E_{J''}+\hbar\omega_{\vec{q}\xi}}\right.$$

$$\left.+\frac{(-1)^{1+t+\lambda}\begin{Bmatrix}t & 1 & \lambda\\ J' & J & J''\end{Bmatrix}\langle iJ\|\,\mathfrak{D}^{(t)}\,\|jJ''\rangle\langle jJ''\|\,\mathfrak{D}^{(1)}\,\|fJ'\rangle}{E_J-E_{J''}-\hbar\omega_{\vec{q}\xi}}\right).$$

We can introduce X by writing this intensity as $\frac{2}{3}(e^2\omega'^4/2\pi c^3)\,X\,d\Omega$; then X is defined as

$$X(f) = \sum_{\vec{s}\vec{q}\xi}\frac{\hbar e^2}{2MNr_0^2\omega_{\vec{q}\xi}}\Big|\sum_{\substack{mn'\\ tp\lambda}} a^{i*}_m a^f_{m'} A_{tp}\langle Jm|\,T^{(\lambda)}_{p+s}\,|J'm'\rangle\Big|^2\delta(\omega_{\vec{q}\xi}-\omega)\,. \tag{3}$$

It is worth noting that both $\mathfrak{D}^{(1)}$ and $\mathfrak{D}^{(t)}$ operate only on the orbital space. The fluorescence lines observed, however, occur between quintets and septets. Consequently, they occur only via breakdown of LS coupling. Since $\zeta\vec{l}\cdot\vec{s}$ does not destroy Jm quantization, this effect can be incorporated into the evaluation of the reduced matrix elements by using the correct linear combination of LS-coupled functions. This will be estimated when we consider every transition separately.

The consequences of symmetry can be found from the cubic harmonic expansion for V where every A_{tp} is replaced by $A_t(\Gamma^{(P)}_p)$; $\Gamma^{(P)}_p$ represents the p partner of the $\Gamma^{(P)}$ irreducible representation. The phonon sum restricts $\sum_{\vec{q}\xi}|A_t(\Gamma^{(P)}_p)|^2$ to be independent of p and then Eq. (3) involves terms of the form

$$\sum_{ifx}\Big|\sum_{jp}(\Gamma^{(I)}_i;\ \Gamma^{(4)}_x\Gamma^{(J)}_j)(\Gamma^{(J)}_j;\ \Gamma^{(P)}_p\Gamma^{(F)}_f)\Big|^2\,,$$

where the sum over degenerate initial and final states appears explicitly with the sum over polarizations as $\sum_{ifx}$. The unitary properties of these cubic coupling coefficients ensure that there will be no cross terms between intermediate states of different symmetry or between potential components of different symmetry. Interference between different multipoles, however, is not excluded.

B. Evaluation of Phonon Potential Field $V(\vec{r}_\alpha\vec{q}\xi)$ and Projected Densities of States

The lattice modes of BaF_2 have been analyzed by means of a simple shell model which has been used to calculate the frequencies ($\omega_{\vec{q}\xi}$) and complex eigenvectors [$\vec{U}_{\vec{q}\xi}(k)$ represent core displacements and $\vec{W}_{\vec{q}\xi}(k)$ relative shell displacements] for traveling waves. They are the solutions of the matrix equations

$$M\omega^2\vec{U} = (R+ZCZ)\vec{U}+(T+ZCY)\vec{W}\,,$$

$$0 = (T+ZCY)^\dagger\vec{U}+(S+YCY)\vec{W}\,,$$

with the usual definitions.[7] R, S, and T represent the short-range ion-ion, shell-shell, and ion-shell interactions, respectively. C specifies the long-range electrostatic interactions and M, Z, Y are diagonal matrices representing the masses, ionic charges, and shell charges, respectively.

The core displacement $\vec{U}(lk)$ of ion k in cell l in a particular mode $\vec{q}\xi$ may be written

$$\vec{U}(lk) = \left(\frac{\hbar}{2M_kN\omega_{\vec{q}\xi}}\right)^{1/2}$$

$$\times[\vec{U}_{\vec{q}\xi}(k)\,a_{\vec{q}\xi}\,e^{+i\vec{q}\cdot(\vec{l}+\vec{k})}+\vec{U}^*_{\vec{q}\xi}a^\dagger_{\vec{q}\xi}\,e^{-i\vec{q}\cdot(\vec{l}+\vec{k})}]\,, \tag{4}$$

where $\vec{l}+\vec{k}$ represents the equilibrium position of ion (lk) and N the number of cells in the crystal. A similar expression exists for the shell displacements.

In evaluating the electrostatic interaction between these charges and the electrons on the samarium ion (situated at $\vec{l}=\vec{k}=0$), we assume that the electrons are centered at the instantaneous position of the ion and that the ion assumes the motion of the original barium ion it replaces. This naive approximation will be questioned later in the light of the results. Nevertheless, it does provide a simple way of calculating the interaction without introducing further unknown parameters.

This interaction with an electron situated at $\vec{r}$ on the samarium ion may be written

$$eV = -|e|^2 {\sum_{lk}}' Z_k \vec{\nabla}_R \left(\frac{1}{|\vec{R}-\vec{r}|}\right)\Big|_0 \cdot [\vec{U}(lk)-\vec{U}(00)] + \text{similar term with } Z_k\vec{U}(lk) \text{ replaced by } Y_k\vec{W}(lk); \quad (5)$$

$\vec{R}\equiv\vec{l}+\vec{k}+\vec{U}(lk)-\vec{U}(00)$ and the derivatives are evaluated for $\vec{U}(lk)=\vec{U}(00)=0$. $\mathcal{H}_{el}$ is obtained by substituting from Eq. (4) into this expression (5) and summing over all $4f$ electrons and lattice modes.

If, further, we now neglect any overlap between these electrons and the ligand ions, we can expand the potential in a multipole series and use selection rules to limit the number of terms required for a given vibronic transition. This expansion is sufficient to specify the A_{tp} parameters introduced via Eq. (2) and the vibronic spectra are finally calculated from Eq. (3). It is convenient to express the expansion in terms of cubic harmonics. When the symmetry properties are considered this procedure results in a small number of independent projected densities of states. The ensuing Brillouin-zone sums can be simplified considerably with the help of a lemma described by Timusk and Klein[8] in which the 48 symmetry elements of O_h are used to generate the complete set of eigenvectors in the Brillouin zone from only a primitive $\frac{1}{48}$ of the zone. The multipoles and associated densities of states can be specified (note that the shell contributions are not explicitly shown).

1. Dipole

The dipole term may be written

$$\sum_\alpha \vec{\nabla}_r(V)|_0 \cdot \vec{r}_\alpha \equiv \Gamma_{4u}(R)\cdot\Gamma_{4u}(r)\ .$$

The lattice-mode sum reduces $|\Gamma_{4u}(R)|^2$ to $(e^2\hbar/2M\omega r_0^6)\rho_1(\Gamma_{4u},\ \omega)$ where

$$\rho_1(\Gamma_{4u},\ \omega)=\frac{1}{3}\left(\frac{r_0^6}{N}\right)\sum_{x,\vec{q},\xi}\left|\sum_{lk}\frac{-Z_k}{(M_k)^{1/2}}\frac{\partial C}{\partial R_x}\,e^{i\vec{q}\cdot\vec{R}}\right|^2 \times\delta(\omega_{\vec{q}\xi}-\omega)\ ,$$

with

$$\vec{R}\equiv\vec{l}+\vec{k},\quad \vec{U}\equiv\vec{U}_{\vec{q}\xi}(k),\quad C\equiv\vec{\nabla}_R(1/|\vec{R}|)\cdot\vec{U},$$

and M_k is expressed in atomic numbers. The sum over components of the irreducible representations is redundant but is included to illustrate the correct normalizations.

2. Quadrupole

Similarly the quadrupole term is

$$\sum_\alpha \frac{1}{2!}\sum_{xy}\frac{\partial^2 V}{\partial x\partial y}\Big|_0 x_\alpha y_\alpha \equiv \Gamma_{3g}(R)\cdot\Gamma_{3g}(r)+\Gamma_{5g}(R)\cdot\Gamma_{5g}(r)\ .$$

$|\Gamma_{3g}(R)|^2$ reduces to $(e^2\hbar/2M\omega r_0^8)\rho_2(\Gamma_{3g},\ \omega)$, where

$$\rho_2(\Gamma_{3g},\ \omega)=\frac{1}{2}\left(\frac{r_0^8}{N}\right)\sum_{\vec{q},\xi}\left[\left|\sum_{lk}\frac{Z_k}{2(3M_k)^{1/2}}\left(2\frac{\partial^2 C}{\partial R_z^2}-\frac{\partial^2 C}{\partial R_x^2}-\frac{\partial^2 C}{\partial R_y^2}\right)e^{i\vec{q}\cdot\vec{R}}\right|^2+\left|\sum_{lk}\frac{Z_k}{2(M_k)^{1/2}}\left(\frac{\partial^2 C}{\partial R_x^2}-\frac{\partial^2 C}{\partial R_y^2}\right)e^{i\vec{q}\cdot\vec{R}}\right|^2\right]\delta(\omega_{\vec{q}\xi}-\omega)$$

and $|\Gamma_{5g}(R)|^2$ reduces to $(e^2\hbar/2M\omega r_0^8)\rho_2(\Gamma_{5g},\ \omega)$, where

$$\rho_2(\Gamma_{5g},\ \omega)=\frac{1}{3}\left(\frac{r_0^8}{N}\right)\sum_{x,y,\vec{q},\xi}\left|\sum_{lk}\frac{Z_k}{(M_k)^{1/2}}\frac{\partial^2 C}{\partial R_x\,\partial R_y}\,e^{i\vec{q}\cdot\vec{R}}\right|^2\delta(\omega_{\vec{q}\xi}-\omega)\ .$$

3. Octupole

The octupole expansion is

$$\sum_\alpha \frac{1}{3!}\sum_{x,y,z}\frac{\partial^3 V}{\partial x\partial y\partial z}\Big|_0 x_\alpha y_\alpha z_\alpha \equiv \Gamma_{2u}(R)\cdot\Gamma_{2u}(r)+\Gamma_{4u}(R)\cdot\Gamma_{4u}(r)+\Gamma_{5u}(R)\cdot\Gamma_{5u}(r)\ .$$

$|\Gamma_{2u}(R)|^2$ reduces to $(e^2\hbar/2M\omega r_0^{10})\rho_3(\Gamma_{2u},\ \omega)$, where

$$\rho_3(\Gamma_{2u},\ \omega)=\left(\frac{r_0^{10}}{N}\right)\sum_{\vec{q},\xi}\left|\sum_{lk}\frac{-Z_k}{(M_k)^{1/2}}\frac{\partial^3 C}{\partial R_x\,\partial R_y\,\partial R_z}\,e^{i\vec{q}\cdot\vec{R}}\right|^2\delta(\omega_{\vec{q}\xi}-\omega)\ ,$$

$|\Gamma_{4u}(R)|^2$ reduces to $(e^2\hbar/2M\omega r_0^{10})\rho_3(\Gamma_{4u},\ \omega)$, where

$$\rho_3(\Gamma_{4u},\ \omega)=\frac{1}{3}\left(\frac{r_0^{10}}{N}\right)\sum_{x,y,z,\vec{q},\xi}\left|\sum_{lk}\frac{-Z_k}{2(15M_k)^{1/2}}\left(\frac{3\partial^3 C}{\partial R_x\,\partial R_y^2}+\frac{3\partial^3 C}{\partial R_x\,\partial R_z^2}-\frac{2\partial^3 C}{\partial R_x^3}\right)(e^{i\vec{q}\cdot\vec{R}}-\delta_{k,0})\right|^2\delta(\omega_{\vec{q}\xi}-\omega)\ ,$$

and $|\Gamma_{5u}(R)|^2$ reduces to $(e^2\hbar/2M\omega r_0^{10})\rho_3(\Gamma_{5u},\ \omega)$, where

$$\rho_3(\Gamma_{5u},\ \omega)=\frac{1}{3}\left(\frac{r_0^{10}}{N}\right)\sum_{x,y,z,\vec{q},\xi}\left|\sum_{lk}\frac{-Z_k}{2(M_k)^{1/2}}\left(\frac{\partial^3 C}{\partial R_x\,\partial R_y^2}-\frac{\partial^3 C}{\partial R_x\,\partial R_z^2}\right)e^{i\vec{q}\cdot\vec{R}}\right|^2\delta(\omega_{\vec{q}\xi}-\omega)\ .$$

The octupole-dipole interference term becomes $(e^2\hbar/2M\omega r_0^8)\rho_{13}(\Gamma_{4u},\omega)$, where

$$\rho_{13}(\Gamma_{4u},\ \omega)=\frac{1}{3}\left(\frac{r_0^8}{N}\right)\sum_{x,y,z,\vec{q},\xi}\left\{\left(\sum_{lk}\frac{-Z_k}{(M_k)^{1/2}}\frac{\partial C}{\partial R_x}\,e^{i\vec{q}\cdot\vec{R}}\right)\left[\sum_{lk}\frac{-Z_k}{2(15M_k)^{1/2}}\left(\frac{3\partial^3 C}{\partial R_x\,\partial R_y^2}+\frac{3\partial^3 C}{\partial R_x\partial R_z^2}-\frac{2\partial^3 C}{\partial R_x^3}\right)(e^{i\vec{q}\cdot\vec{R}}-\delta_{k,0})\right]^*\right.$$
$$\left.+\text{complex conjugate}\right\}\delta(\omega_{\vec{q}\xi}-\omega)\ .$$

$\delta_{k,0}$ is zero unless k refers to the barium site; then its value is unity.

All terms in $\vec{U}(00)$ vanish in cubic symmetry with the exception of that from the octupole Γ_{4u}. The samarium ion, moving in a rigid cubic lattice, will experience an octupole interaction which is just this term. Consequently, this is the only contribution which depends directly on the motion of the impurity ion. Further multipoles are not relevant to experiments which involve a maximum change in J of 2.

The lattice sums were evaluated on a computer using the Ewald method[9] and the projections are shown in Figs. 1–9. The separate phonon contribution, from the ion motion only, is also explicitly displayed for the dipole term to help in elucidating the structure of that projected density of states. The projections $\rho(\nu)\Delta\nu/\nu$ are drawn for $\delta\nu=\nu_{\max}/100=9.677\times10^{10}$ Hz.

C. Transition $^5D_0\rightarrow{}^7F_0$

The only contributions to this sideband arise from $\lambda=0$ with $p=-s$. Equation (2) will restrict t to being 1 and we are led to the usual result that *only* the uniform electric field produced by the phonons will contribute to the intensity of this vibronic sideband.

$X(^7F_0)$ as defined by Eq. (3) becomes

$$\sum_s\sum_{\vec{q}\xi}\left(\frac{e^2\hbar}{2MNr_0^2\omega_{\vec{q}\xi}}\right)|A_{1s}\langle 00|\,T_0^{(0)}\,|00\rangle|^2\delta(\omega_{\vec{q}\xi}-\omega)\ .$$

Inserting the appropriate density of states this becomes

$$\frac{1}{3}\left(\frac{e^4\hbar}{2Mr_0^6\omega}\right)|\langle 0\|\,T^{(0)}\,\|0\rangle|^2\rho_1(\Gamma_{4u},\ \omega)\ ,$$

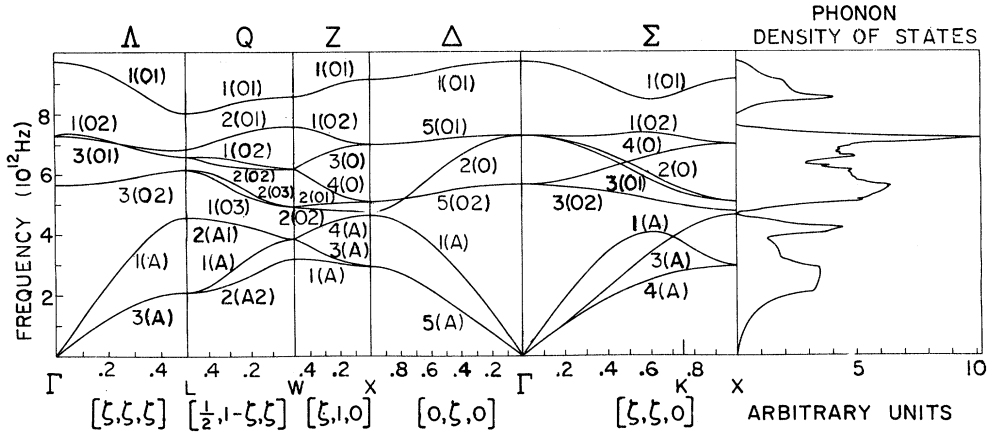

FIG. 1. Calculated dispersion curves for lattice modes of BaF_2 and associated density of states.

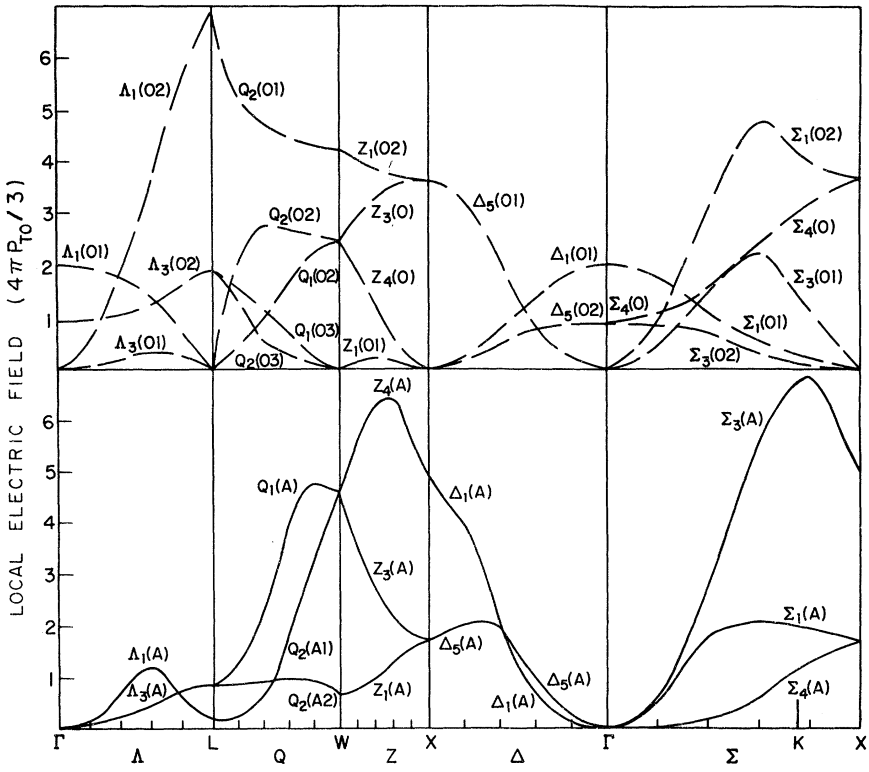

FIG. 2. Separate phonon contributions to the projected dipole (Γ_{4u}) density of states (ion contribution only). P_{TO} represents the lattice polarization in the infrared-active TO mode.

with

$$\langle 0 \| T^{(0)} \| 0 \rangle = \sum_j \langle i0 \| \mathfrak{D}^{(1)} \| j1 \rangle \langle j1 \| \mathfrak{D}^{(1)} \| f0 \rangle \times \left(\frac{1}{E(^5D_0) - E(j) - \hbar\omega} + \frac{1}{E(^7F_0) - E(j) + \hbar\omega} \right).$$

The sum over intermediate states j only involves those states with $J = 1$.

We estimate the value of this reduced matrix element in the following way: We assume a splitting Δ between quintets and septets in both the f^6 and f^5d configurations of 10 000 cm^{-1}. Also the

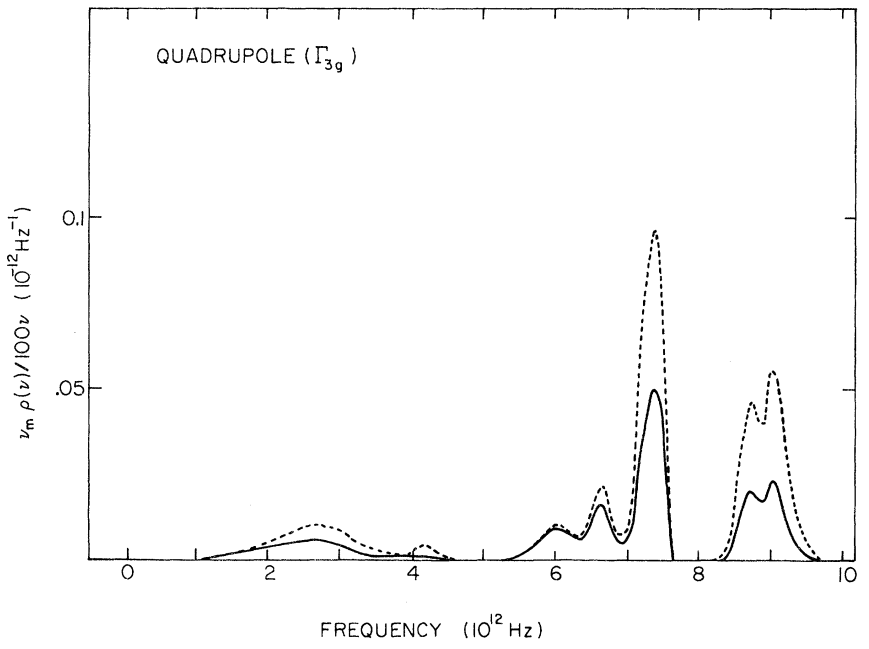

FIG. 3. Projected quadrupole (Γ_{3g}) density of states. Solid line: ion contribution; dashed line: ion plus shell contributions.

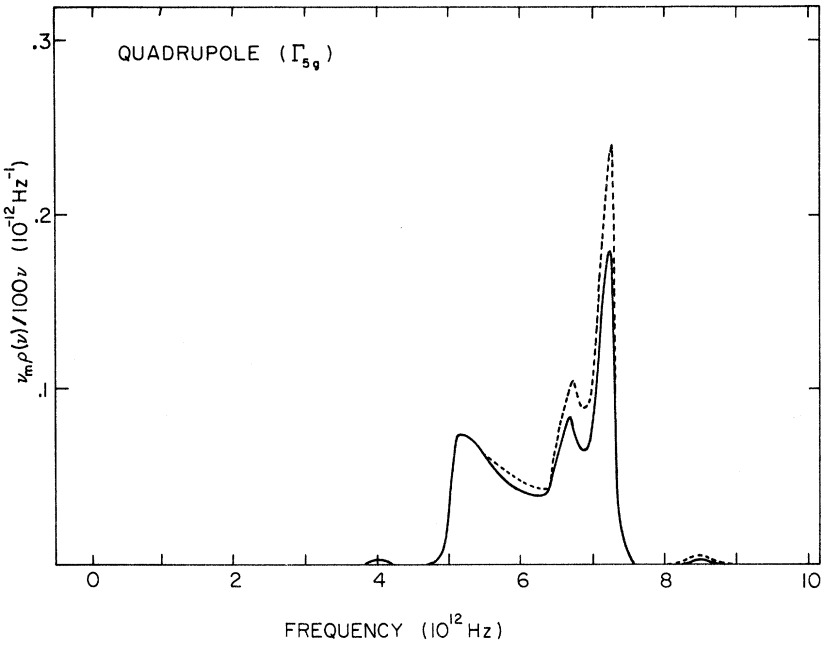

FIG. 4. Projected quadrupole (Γ_{5g}) density of states (rest as for Fig. 3).

proximity of the excited configurations causes $E(j) - E(^5D_0)$ to be of order Δ. Then

$$\langle 0 \| T^{(0)} \| 0 \rangle \sim (4f|r|5d)^2 \zeta/\Delta^2 hc . \quad (6)$$

We obtain a value for ζ from our results of 1590 ± 50 cm^{-1}, the uncertainty again arising from breakdown of LS coupling. The value of $(4f|r|5d)$ can be estimated from the $5d$ functions for Pr^{3+} and Tm^{3+}, calculated by Rajnak.[10] Interpolating between these ions, we derive a value of $0.8a_0$ (0.42 Å) for Sm^{2+}. The results of Freeman and Watson[11] would seem to indicate that this estimate, based on values for trivalent ions, should not be in error by more than 10%. Finally, we obtain for $X(^7F_0)$

$$\frac{1}{3}\left(\frac{e^2\zeta(f|r|d)^2}{\Delta^2 r_0^2 hc}\right)^2 \left(\frac{\hbar}{2M\omega r_0^2}\right) \rho_1(\Gamma_{4u}, \omega) . \quad (7)$$

This has a value $1.25\times 10^{-8}\,\rho_1(\Gamma_{4u}, \omega)/\omega$ cm^2/(rad/

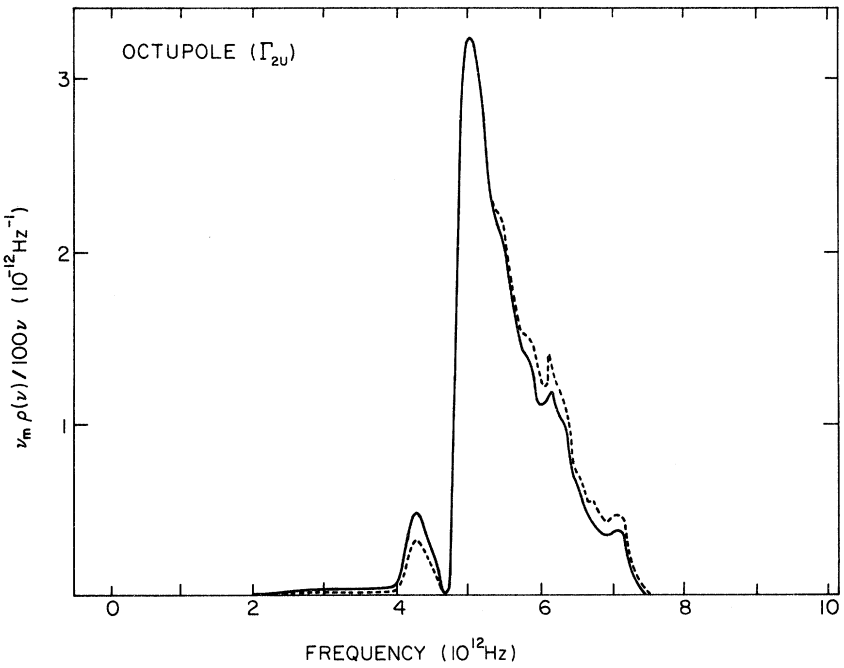

FIG. 5. Projected octupole (Γ_{2u}) density of states (rest as for Fig. 3).

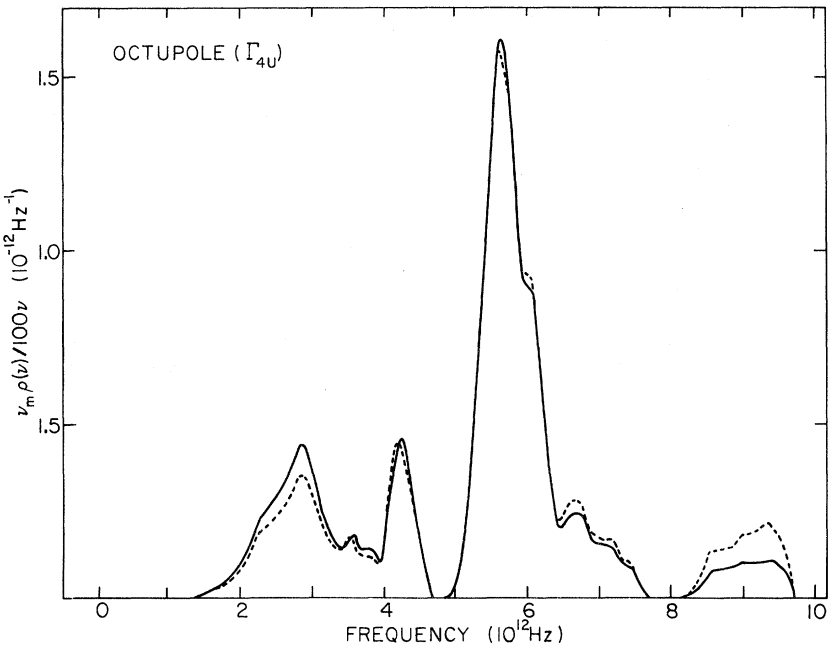

FIG. 6. Projected octupole (Γ_{4u}) density of states (rest as for Fig. 3).

sec).

D. Transition $^5D_0 \rightarrow {}^7F_1$

Contributions to this electric-dipole sideband arise from $\lambda = 1$ and $p + s = -m'$. Both $t = 1$ and 2 would contribute, but 2 corresponds to the quadrupole interaction; its even parity precludes any contribution to this sideband and we are left once again with only the uniform electric field. Consequently, the sideband shape should be similar to that for the previous transition with $X(^7F_1)$ given by

$$\sum_{sm'} \sum_{\vec{q}\xi} \left(\frac{e^2\hbar}{2MNr_0^6 \omega_{\vec{q}\xi}} \right) \left| \sum_p A_{1p} \langle 00 | T^{(1)}_{p+s} | 1m' \rangle \right|^2 \delta(\omega_{\vec{q}\xi} - \omega)$$

$$= \frac{1}{3} \left(\frac{e^4\hbar}{2Mr_0^6 \omega} \right) |\langle 0 \| T^{(1)} \| 1 \rangle|^2 \rho_1(\Gamma_{4u}, \omega) , \quad (8)$$

with

$$\langle 0 \| T^{(1)} \| 1 \rangle = \sum_j \langle i0 \| \mathfrak{D}^{(1)} \| j1 \rangle \langle j1 \| \mathfrak{D}^{(1)} \| f1 \rangle$$

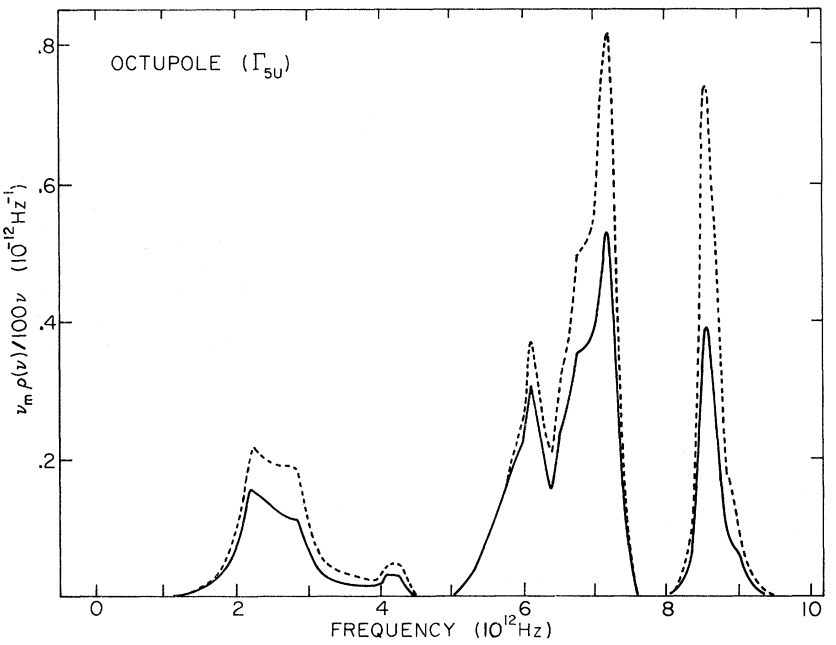

FIG. 7. Projected octupole (Γ_{5u}) density of states (rest as for Fig. 3).

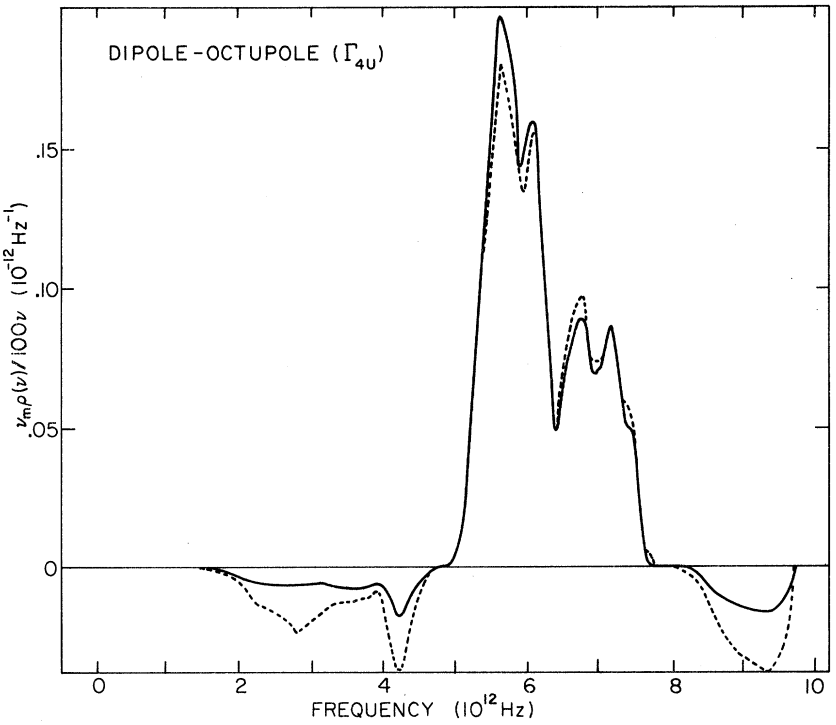

FIG. 8. Projected dipole-octupole (Γ_{4u}) interference density of states (rest as for Fig. 3).

$$\times\left(\frac{1}{E(^5D_0)-E(j)-\hbar\omega}-\frac{1}{E(^7F_0)-E(j)+\hbar\omega}\right).$$

The sum over intermediate states j only involves those states with $J=1$.

The reduced matrix element now contains the difference of the two terms in the last large parentheses. The proximity of the f^5d configuration, however, should enhance the first term considerably over the second, resulting in the difference being about $\frac{1}{3}$ of their sum. The cancellation for higher intermediate states is virtually complete. Hence $X(^7F_1)$ for this vibronic is similar to Eq. (7), but reduced by at least an order of magnitude.

The parent electronic transition is a strong

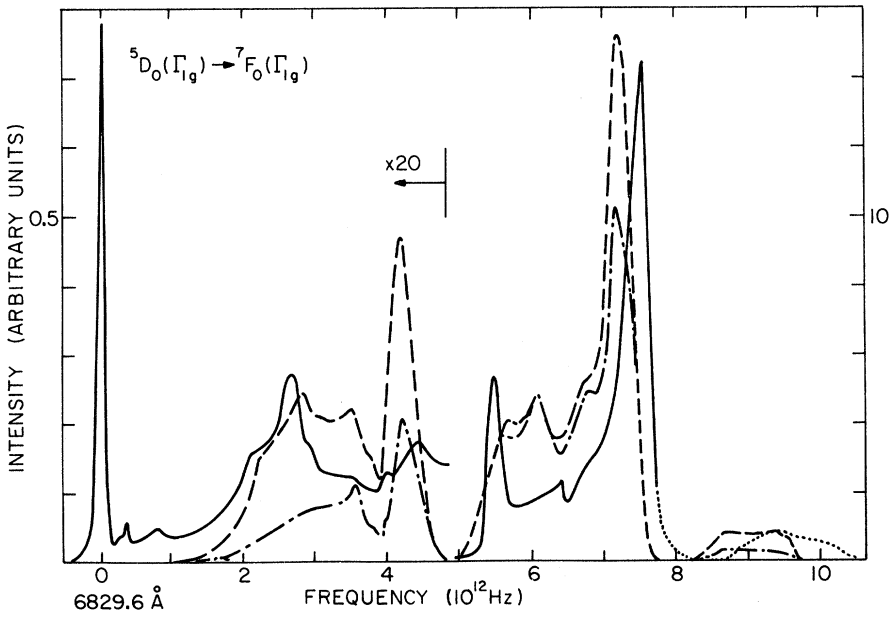

FIG. 9. Vibronic spectrum accompanying $^5D_0 \rightarrow {}^7F_0(\Gamma_{1g})$. Solid line: experiment; dot-dashed line: ion contribution; dashed line: ion plus shell contribution.

magnetic-dipole (MD)-allowed transition and permits the possibility of a significant MD sideband contribution. The parent transition also occurs by breakdown of LS coupling. Writing explicitly the important terms and noting that the transition probability is isotropic, we obtain an effective $X^0(^7F_1)$ of

$$(\mu_B/e)^2 \left| \langle {}^5D_0^{(1)} + \mu\, {}^7F_0 \| L+2S \| {}^7F_1 - \nu\, {}^5D_1^{(1)} \rangle \right|^2 g(\omega),$$

where $g(\omega)$ represents the line profile with $\int g(\omega)\, d\omega = 1$, μ_B is the Bohr magneton,

$$\mu = \langle {}^7F_0 | \textstyle\sum_\alpha \vec{l}_\alpha \cdot \vec{s}_\alpha | {}^5D_0^{(1)} \rangle \, (\zeta/\Delta),$$

and

$$\nu = \langle {}^7F_1 | \textstyle\sum_\alpha \vec{l}_\alpha \cdot \vec{s}_\alpha | {}^5D_1^{(1)} \rangle \, (\zeta/\Delta).$$

Only the lowest $^5D^{(1)}$ multiplet contributes because

$$(\gamma SLJ \| L+2S \| \gamma' L' S' J+1) = \delta(\gamma\gamma')\, \delta(LL')\, \delta(SS')(-1)^{L+S+J} [(2J+1)(2J+3)]^{1/2} \begin{Bmatrix} S & J & L \\ J+1 & S & 1 \end{Bmatrix} (S \| S \| S),$$

where

$$(S \| S \| S) = [S(S+1)(2S+1)]^{1/2}.$$

Also we have

$$\frac{(^7F_0 | \textstyle\sum_\alpha \vec{l}_\alpha \cdot \vec{s}_\alpha | {}^5D_0)}{(^7F_1 | \textstyle\sum_\alpha \vec{l}_\alpha \cdot \vec{s}_\alpha | {}^5D_1)} = \begin{Bmatrix} 0 & 3 & 3 \\ 1 & 2 & 2 \end{Bmatrix} \begin{Bmatrix} 1 & 3 & 3 \\ 1 & 2 & 2 \end{Bmatrix}^{-1} = \frac{3\sqrt{2}}{4}$$

and, assuming hydrogenic-radial functions, we can use the results of Judd[12] for europium salts to estimate that

$$(^7F_1 | \textstyle\sum_\alpha \vec{l}_\alpha \cdot \vec{s}_\alpha | {}^5D_1^{(1)}) = -3.1 \ .$$

Then $X^0(^7F_1)$ reduces to

$$\tfrac{3}{2}(\mu_B/e)^2 (3.1\zeta/\Delta)^2 g(\omega). \tag{9}$$

This has a value $(1.36 \times 10^{-22}) g(\omega)$ cm^2/(rad/sec).

The MD sideband occurs via the quadrupole interaction which possesses a diagonal term, as described in the introduction to this section, in the final $^7F_1$ states. So long as the coupling remains weak, this "oscillator shift" can be treated in our perturbation approximation and Eq. (2) can be used with $\lambda = 1$, $p+s = -m'$, and $t = 2$ to give

$$X^1(^7F_1) = \sum_{sm'} \sum_{\vec{q}\xi} \left(\frac{e^2\hbar}{2MNr_0^2\omega_{\vec{q}\xi}} \right) \left| \sum_p A_{2p} \langle 00 | \, T^{(1)}_{p+s} \, | lm' \rangle \right|^2 \delta(\omega_{\vec{q}\xi} - \omega),$$

with

$$\langle 00 | \, T^{(1)}_{p+s} \, | lm' \rangle = \sqrt{3} \left(\frac{\mu_B}{e} \right) \begin{pmatrix} 1 & 2 & 1 \\ s & p & m' \end{pmatrix} \begin{Bmatrix} 1 & 2 & 1 \\ 1 & 0 & 1 \end{Bmatrix} \frac{\langle {}^5D_0 \| L+2S \| {}^7F_1 \rangle \langle {}^7F_1 \| \mathfrak{D}^{(2)} \| {}^7F_1 \rangle}{\hbar\omega_{\vec{q}\xi}}.$$

Using the appropriate densities of states this becomes

$$\left(\frac{\mu_B{}^2}{15e^2} \right) \left(\frac{e^2 |\langle 0 \| T^{(1)} \| 1 \rangle|}{\hbar\omega r_0^3} \right)^2 \left(\frac{\hbar}{2M\omega r_0^2} \right) [\rho_2(\Gamma_{3g}, \omega) + \tfrac{8}{9} \rho_2(\Gamma_{5g}, \omega)], \tag{10}$$

with

$$\langle 0 \| T^{(1)} \| 1 \rangle \equiv \langle {}^5D_0 \| L+2S \| {}^7F_1 \rangle \langle {}^7F_1 \| \mathfrak{D}^{(2)} \| {}^7F_1 \rangle.$$

We have

$$(\gamma SLJ \| \mathfrak{D}^{(2)} \| \gamma SLJ) = (-1)^{S+L+J} (2J+1) \begin{Bmatrix} L & J & S \\ J & L & 2 \end{Bmatrix} \times (f \| r^2 C^{(2)} \| f) (\gamma SL \| U^2 \| \gamma SL),$$

with $(33 \| U^2 \| 33) = -1$ from the tables of Nielson and Koster.[13] Hence

$$\langle {}^7F_1 \| \mathfrak{D}^{(2)} \| {}^7F_1 \rangle = -(\tfrac{3}{10})^{1/2} (f | r^2 | f).$$

Apart from the different density-of-states functions, this sideband intensity is reduced by a factor

$$\tfrac{1}{50} \, (e^2 \langle r^2 \rangle / \hbar\omega r_0^3)^2 \, (\hbar / 2M\omega r_0^2) \tag{11}$$

from its parent electronic (MD) transition. Wagner[1] has shown for acoustic phonons that $\rho_1(\omega) \propto \omega^6$, while $\rho_2(\omega) \propto \omega^4$. Consequently, this sideband intensity is proportional to ω as $\omega \to 0$, but the electric dipole sideband is proportional to ω^5.

We can estimate $\langle r^2 \rangle$ from the tables of Freeman and Watson[11] to be a_0^2 and then this reduction factor becomes $1.1/\nu^3$, where $\nu = \omega/2\pi$ and is expressed in units of 10^{12} Hz.

E. Transitions $^5D_0 \rightarrow {}^7F_2$ (Γ_{3g} and Γ_{5g})

The static-cubic crystal field splits the $^7F_2$ multiplet into Γ_{3g} and Γ_{5g} states with a splitting of 308 cm^{-1}. Contributions to these electric-dipole sidebands arise from $\lambda = 2$ and $t = 1, 3$: Parity excludes $t = 2$ and we are left with dipole and octupole contributions.

A look at the symmetry exposes two special features of these transitions. While the dipole contributes to both $^7F_2(\Gamma_{3g})$ and $^7F_2(\Gamma_{5g})$ transitions and all components of the octupole contribute to the $^7F_2(\Gamma_{5g})$ transition, only the Γ_{4u} and Γ_{5u} octupole components contribute to $^7F_2(\Gamma_{3g})$. Secondly, since both dipole and octupole moments possess Γ_{4u} symmetry, the intensities will possess an interference term between the two multipoles. This term has opposite sign for $^7F_2(\Gamma_{3g})$ and $^7F_2(\Gamma_{5g})$ but equal magnitude in our approximation.

A straightforward substitution of the densities of states together with the explicit form of the eigenvectors for the $^7F_2$ multiplet gives for the $^7F_2(\Gamma_{3g})$ transition

$$X(\Gamma_{3g}) = \frac{1}{1575}\left(\frac{e^4\hbar}{2M\omega r_0^2}\right)\left(\frac{210}{r_0^4}\,|\langle 0\|T^{(2)}_{\rm dip}\|2\rangle|^2\rho_1(\Gamma_{4u},\omega) + \frac{3\sqrt{210}}{r_0^6}\langle 0\|T^{(2)}_{\rm dip}\|2\rangle\langle 2\|T^{(2)}_{\rm oct}\|0\rangle\rho_{13}(\Gamma_{4u},\omega) + \frac{1}{r_0^8}\,|\langle 0\|T^{(2)}_{\rm oct}\|2\rangle|^2[9\rho_3(\Gamma_{4u},\omega)+5\rho_3(\Gamma_{5u},\omega)]\right), \quad (12)$$

with

$$\langle 0\|T^{(2)}_{\rm dip}\|2\rangle \equiv \sum_j \langle 0\|\mathfrak{D}^{(1)}\|j1\rangle\langle j1\|\mathfrak{D}^{(1)}\|2\rangle\left(\frac{1}{E(^5D_0)-E(j)-\hbar\omega} + \frac{1}{E(^7F_2)-E(j)+\hbar\omega}\right)$$

and

$$\langle 0\|T^{(2)}_{\rm oct}\|2\rangle \equiv \sum_j \left(\frac{\langle 0\|\mathfrak{D}^{(1)}\|j1\rangle\langle j1\|\mathfrak{D}^{(3)}\|2\rangle}{E(^5D_0)-E(j)-\hbar\omega} + \frac{(\frac{3}{7})^{1/2}\langle 0\|\mathfrak{D}^{(3)}\|j3\rangle\langle j3\|\mathfrak{D}^{(1)}\|2\rangle}{E(^7F_2)-E(j)+\hbar\omega}\right).$$

Also for the $^7F_2(\Gamma_{5g})$ transition the following is obtained:

$$X(\Gamma_{5g}) = \frac{1}{1575}\left(\frac{e^4\hbar}{2M\omega r_0^2}\right)\left(\frac{315}{r_0^4}\,|\langle 0\|T^{(2)}_{\rm dip}\|2\rangle|^2\rho_1(\Gamma_{4u},\omega) - \frac{3\sqrt{210}}{r_0^6}\langle 0\|T^{(2)}_{\rm dip}\|2\rangle\langle 2\|T^{(2)}_{\rm oct}\|0\rangle\rho_{13}(\Gamma_{4u},\omega) + \frac{1}{r_0^8}\,|\langle 0\|T^{(2)}_{\rm oct}\|2\rangle|^2[5\rho_3(\Gamma_{2u},\omega)+6\rho_3(\Gamma_{4u},\omega)+10\rho_3(\Gamma_{5u},\omega)]\right). \quad (13)$$

If the $^7F_2(\Gamma_{3g})$ and $^7F_2(\Gamma_{5g})$ intensities are added, the cross terms cancel and the total octupole contribution becomes proportional to

$$\rho_3(\Gamma_{2u}) + 3\rho_3(\Gamma_{4u}) + 3\rho_3(\Gamma_{5u}).$$

This result is similar to the sum rule derived by Judd[5] for the intensities of rare-earth transitions in liquids. When $\langle 0\|T^{(2)}_{\rm dip}\|2\rangle/r_0^2$ is greater than $\langle 0\|T^{(2)}_{\rm dip}\|2\rangle/r_0^4$, the octupole contribution to the separate intensities will be dominated by the cross term. In the same approximation used to derive Eqs. (6) and (7),

$$\frac{r_0^2\langle 0\|T^{(2)}_{\rm dip}\|2\rangle}{\langle 0\|T^{(2)}_{\rm oct}\|2\rangle} \approx \frac{r_0^2(4f|r|5d)}{(4f|r^3|5d)} \sim 5, \quad (14)$$

assuming $(4f|r^3|5d) \sim 6a_0^3$.

The complicated $^7F_2$ vibronics which, in general, require seven parameters for a multipole fit are now described by only two parameters.

III. EXPERIMENT

The vibronic spectra were observed at 4.2 °K with a resolution of 1 cm^{-1} using a 1-m Jarrell-Ash spectrometer. The fluorescence was excited by a filtered Hg-Xe 1000-W lamp and detected with an EMI model No. 9558B photomultiplier tube. Excitation was achieved occasionally with a He-Ne laser.

The data were reduced to a linear frequency scale before the presentation in Figs. 9–12. The dotted regions refer to overlapping sections from different J levels. The dashed curves are the result of plotting the theoretical curves of Sec. II. Their heights have been arbitrarily adjusted within the limits imposed by the theory and will be compared with the estimates of the intensities normalized to the no-phonon $|^5D_0\rangle \rightarrow |^7F_1\rangle$ transition. The width of this transition at half-intensity is 5 cm^{-1}, with the peak intensity given by $g(0) = 2/\pi\gamma$ assuming a Lorentzian line shape, and $\gamma = 3\pi \times 10^{11}$ rad/sec. We have made no allowance for the di-

electric properties of the host lattice, nor the frequency response of the photocathode.

A. Transition $^5D_0 \rightarrow {}^7F_0$

In view of the selection rules for this transition, the sideband should exactly reflect the electric field produced by the phonons. Whether or not the shell displacements are included in the calculation, Fig. 9 shows that the predicted shape is similar to the experimental results. Certain features such as the [100], $[\frac{3}{4}\ \frac{3}{4}\ 0]$, and $[\frac{1}{2}\ \frac{1}{2}\ \frac{1}{2}]$ critical points for the acoustic phonons are accurately reproduced though the two sharp peaks from the optical phonons show significant deviations; the lower peak is absent in the calculated curves while the higher-frequency peak occurs at too low a frequency. It is tempting to use anharmonic effects to explain this frequency discrepancy; the neutron data were obtained at room temperature while the vibronics were recorded at helium temperature. In Sec. IV we show that this explanation must be pursued with caution. The sharp lower-frequency peak occurs at the frequency of the TO phonon responsible for the reststrahl. This phonon also contributes strongly to the octupole Γ_{4u} potential and consequently other transitions possess a peak in this region of the spectrum also; the dipole potential, however, only possesses a weak contribution through the $\frac{4}{3}\pi\vec{P}$ factor weighted by a relatively low density of states. ($\vec{P}$ is the lattice polarization generated by this $k \approx 0$ phonon.) Consequently, we are forced to assume that our calculation does not adequately predict this feature. The possibility of a resonance or incipient resonance mode is attractive but must be confirmed by a Green's-function calculation. It is also worth noting that the shell displacements give a positive contribution in this region but a negative contribution to most of the rest of the sideband.

In general, the acoustic phonons and the high-frequency phonon branch only contribute weakly to the dipolar potential. This is demonstrated in Fig. 2 where it can be seen that contributions from zone-boundary phonons exceed the $\frac{8}{3}\pi\vec{P}$ field from the LO phonon by a factor of 4. Consequently, this potential is dominated by the zone-boundary phonons and hence by short-range contributions. Since the latter are likely to be the least successfully represented by this model, serious discrepancies may appear. For example, the peak between 4×10^{12} and 4.5×10^{12} Hz, which experimentally is weaker and broader, is dominated by the acoustic phonons at the zone boundary, where also the positive ion is moving with large amplitude.

Normalized to the peak intensity of the $^5D_0 \rightarrow {}^7F_1$ MD transition, this sideband should have an intensity given by the ratio of Eq. (7) to Eq. (9), namely,

$$\frac{(1.25\times10^{-8})\rho_1(\Gamma_{4u},\omega)/\omega}{(1.36\times10^{-22})g(0)} = (36\times10^{12})\left(\frac{\rho_1(\Gamma_{4u},\nu)\nu_M}{100\nu}\right).$$

The experimental value for the intensity factor is $\sim 300\times10^{12}$.

B. Transition $^5D_0 \rightarrow {}^7F_1$

Apart from the MD contribution, this sideband possesses identical selection rules to the previous transition $^5D_0 \rightarrow {}^7F_0$. Consequently, its shape should also be similar. The low-frequency contribution (shown dotted) is uncertain because it overlaps the high-frequency phonon contribution to the $^7F_0$ sideband.

The relative intensity of the MD sideband to the zero-phonon transition is given by relation (11), suitably weighted by the appropriate densities of states, and becomes

$$\frac{1.1\times10^{36}}{\nu^3 g(0)}\left[\rho_2(\Gamma_{3g},\omega)+\tfrac{8}{9}\rho_2(\Gamma_{5g},\omega)\right]$$

$$= 2.7\times10^{36}\left(\frac{\rho_2(\Gamma_{3g},\nu)\nu_M}{100\nu^3}+\frac{8}{9}\frac{\rho_2(\Gamma_{5g},\nu)\nu_M}{100\nu^3}\right).$$

The calculated ratio of $1.1/\nu^3$ implies that perturbation theory cannot be strictly used for the contribution of the lower-frequency phonons. We may hope, however, that their low effective densities of states may yield an over-all sideband shape which is not a bad approximation, even though the low-frequency region will be in error.

When this is added to the electric-field contribution as indicated in Fig. 10, the agreement between theory and experiment is as good as for the previous transition; a slight broadening of the features is consistent with a broader zero-phonon transition. The anomalous peak at 5.5×10^{12} Hz is more prominent and shows further structure; also the higher peak remains 10 cm^{-1} above the calculated position. The intensity of the sideband is about ten times weaker than the previous $^7F_0$ sideband, a result which is well predicted by Eq. (8) and its ensuing discussion.

C. Transitions $^5D_0 \rightarrow {}^7F_2$

These two transitions provide a severe test for the simple coupling model, especially with the restrictions imposed by the partial closure which reduces the analysis to a two-parameter fit. The situation is further complicated by the dominating feature at 5.5×10^{12} Hz, which now coincides with the major contribution from the octupole Γ_{4u} potential. When this peak is fitted by a large octupole contribution, the agreement with the rest of the spectrum suffers. In view of the anomalous nature of this peak, we have preferred to force a better fit to the rest of the spectrum by reducing the octupole contribution. Even so, the ratio of dipole to octupole

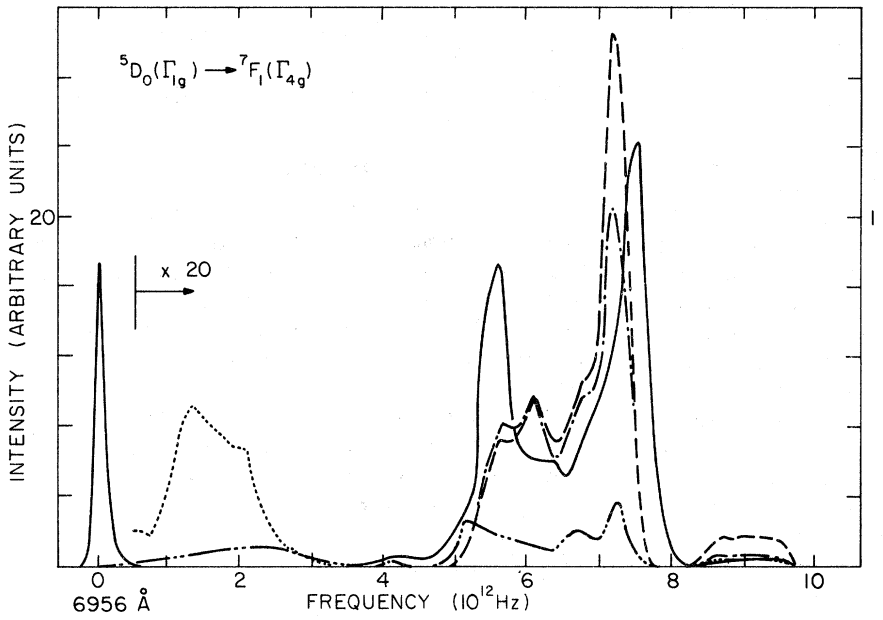

FIG. 10. Vibronic spectrum accompanying $^5D_0 \rightarrow {}^7F_1(\Gamma_{4g})$. Solid line: experiment; dotted line: overlapping region; dot-dashed line: ion contribution; dashed line: ion plus shell contribution; double-dot-dashed line: ion contribution to magnetic-dipole sideband.

contributions

$$r_0^4 \, | \langle 0 \| T_1^{(2)} \| 2 \rangle \langle 0 \| T_3^{(2)} \| 2 \rangle^{-1} |^2$$

becomes 2, whereas the theoretical estimate of relation (14) is $(r_0^2 \langle r \rangle / \langle r^3 \rangle)^2 = 25$. The curves shown in Figs. 11 and 12 have been calculated for a negative contribution of the cross term to $^7F_2(\Gamma_{3g})$. Unfortunately, the fit is not sufficiently accurate to make this sign determination definitive, though the agreement is improved with this sign. Also if we assume the reduced matrix element $\langle 0 \| T_{\mathrm{dip}}^{(2)} \| 2 \rangle$ has the same value as $\langle 0 \| T^{(0)} \| 0 \rangle$ for the $^7F_0$ sideband, these $^7F_2$ sidebands should be an order of magnitude more intense than found experimentally. (This discrepancy is reduced when allowance is made for the photocathode response.)

One significant feature of these spectra is the extra contribution of $\rho_3(\Gamma_{2u}, \omega)$ to the $^7F_2(\Gamma_{5g})$ sideband. It can be seen from Fig. 5 that this density of states possesses a relatively sharp peak at

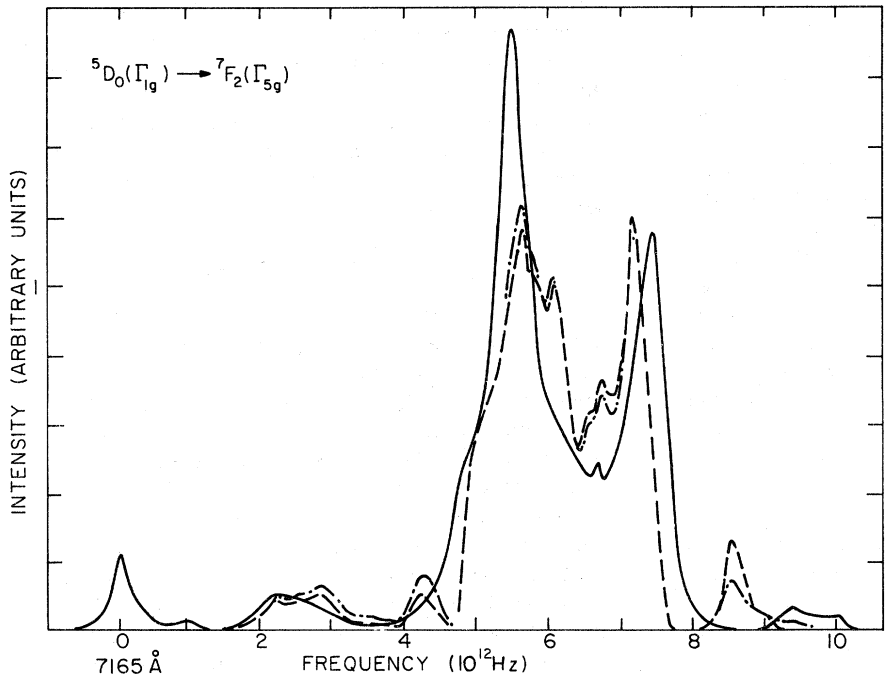

FIG. 11. Vibronic spectrum accompanying $^5D_0 \rightarrow {}^7F_2(\Gamma_{5g})$ (rest as for Fig. 9).

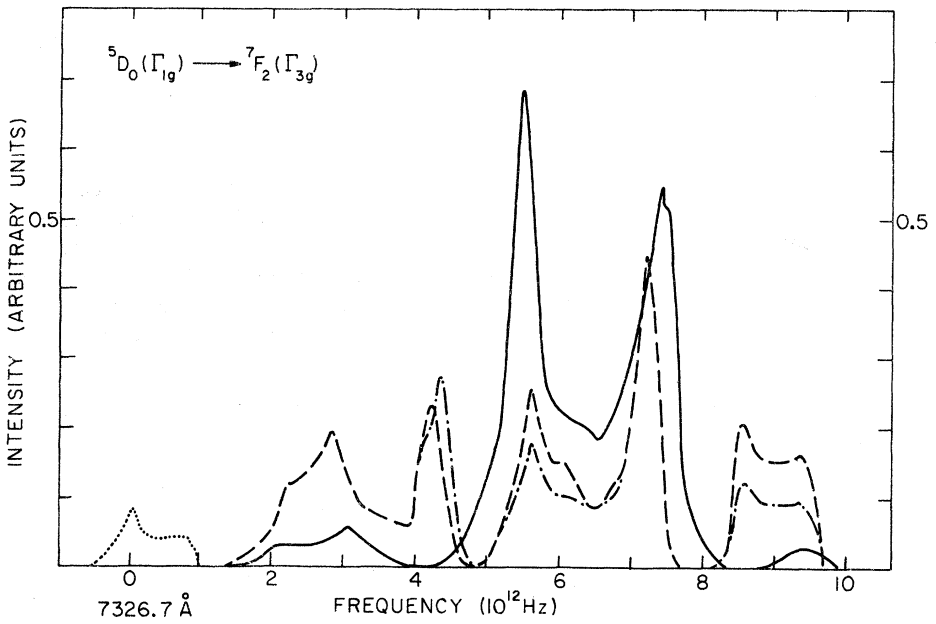

FIG. 12. Vibronic spectrum accompanying $^5D_0 \rightarrow {}^7F_2(\Gamma_{3g})$ (rest as for Fig. 9).

5.0×10^{12} Hz from zone-boundary phonons, which appears as a shoulder on the low-frequency side of the anomalous peak. Another feature is the approximate twofold difference in intensities of these two sidebands, a result which is accommodated by the present theory. (This difference is reduced by 30% when allowance is made for the photocathode response.)

IV. DISCUSSION

In view of the lack of complete agreement, it is pertinent to inquire into some of the possible sources of error in these model calculations. In general, we have four discrepancies to consider: (a) the anomalous peak at 5.5×10^{12} Hz, (b) inaccurate contributions from zone-boundary phonons, (c) frequency deviations of ~ 3% in the position of peak contributions, and (d) a Y_3 contribution 3.5 times larger than predicted. It is natural to ascribe these discrepancies to the lack of a Green's-function calculation to predict the correct excitations for the impure crystal. Certainly the success of the present analysis is sufficiently high that this calculation could be successfully evaluated. There are indications, however, from (c) and (d) that covalent contributions and anharmonic effects also will be significant.

The shell-model parameters are derived from the neutron data gathered at room temperature. No allowance has been made in the calculations for the anharmonic contributions to both the phonon frequencies and their eigenvectors. Table I lists the room-temperature and liquid-nitrogen-temperature properties of $k=0$ phonons. It can be seen that anharmonicities contribute about 5% to these values, certainly sufficient to account for discrepancy (c). We have made no attempt to modify the parameters to allow for these contributions because no simple force-constant change is adequate to fit all the variations listed in the table.

The electric-dipole sidebands arise from matrix elements of the crystal potential between $4f$ and $5d$ electrons. While there exist estimates of shielding,[14] overlap, and covalency[15] in rare-earth static-crystal-field splittings involving the even harmonics in the potential expansion and the $4f$ shell, no such estimates are available for either the $5d$ electrons or the off-diagonal elements required here. Even for the $4f$ shell, it is found that shielding effects of the $5s$ and $5p$ electrons may change the effective potential by as much as 50% depending upon the order of the polynomial,[14] while overlap effects

TABLE I. Comparison of room-temperature and liquid-nitrogen-temperature values for elastic constants, TO phonon (ν_{TO}), and Raman phonon (ν_R) frequencies.

	300 °K	77 °K
$C_{11}(10^{11}$ dyn/cm$^2)$	8.91	9.8[a]
$C_{12}(10^{11}$ dyn/cm$^2)$	4.00	4.45[a]
$C_{44}(10^{11}$ dyn/cm$^2)$	2.54	2.54[a]
ν_{TO}(cm^{-1})	184	192[b]
ν_R(cm^{-1})	240	249[c]

[a]D. Gerlich, Phys. Rev. 135, A1331 (1964).
[b]H. W. Verleur and A. S. Barker, Phys. Rev. 164, 1169 (1967).
[c]P. Rao and S. P. S. Porto (private communication).

may contribute a similar amount to the observed splittings. The radial functions of Rajnak[10] indicate that overlap contributions for $5d$ electrons will certainly be more important than for $4f$ electrons and may be comparable to the values encountered in the $3d$ transition-metal complexes; also the off-diagonal elements will be modified. Under these conditions, all the short-range contributions to the potential from the nearest-neighbor fluorine ions ought to be considered separately and a cluster calculation used to project out the contributions from every phonon. This will modify the contributions to Y_1 from phonons away from the Γ point, but the effect on Y_3 will be more serious. Nevertheless, the present calculations give a clear indication of the reasonable degree of accuracy to be expected from a crystal-field calculation. Our approximations have yielded values for the amplitudes of the multipole contributions within a factor of 3 of the experimental values, though more serious discrepancies of the same magnitude remain in the frequency dependence of some of these terms.

*Research supported by the Joint Services Electronics Program, through the Air Force Office of Scientific Research (AFSC), under Contract No. F 44620-71-C-0067.

†Work supported in part by Volkswagen Foundation.

[1]M. Wagner, Z. Physik 214, 78 (1968).

[2]D. L. Wood and W. Kaiser, Phys. Rev. 126, 2079 (1962).

[3]H. V. Laver, D. H. Kuhner, and W. E. Bron, Bull. Am. Phys. Soc. 16, 427 (1971).

[4]J. P. Hurrell and V. J. Minkiewicz, Solid State Commun. 8, 463 (1970).

[5]B. R. Judd, Phys. Rev. 127, 750 (1962).

[6]J. D. Axe, Phys. Rev. 136, 43 (1964).

[7]R. A. Cowley, W. Cochran, B. N. Brockhouse, and A. D. B. Woods, Phys. Rev. 131, 1020 (1963).

[8]T. Timusk and M. V. Klein, Phys. Rev. 141, 664 (1966).

[9]R. A. Cowley, Acta. Cryst. 15, 687 (1962).

[10]K. Rajnak, J. Chem. Phys. 37, 2440 (1962).

[11]A. J. Freeman and R. E. Watson, Phys. Rev. 127, 2058 (1962).

[12]B. R. Judd, Proc. Roy. Soc. (London) 228A, 120 (1955).

[13]C. W. Nielson and G. F. Koster, *Spectroscopic Coefficients for the p^n, d^n and f^n Configurations* (MIT Press, Cambridge, Mass., 1963).

[14]A. J. Freeman and R. E. Watson, Phys. Rev. 139, 1606 (1965).

[15]A. J. Freeman and R. E. Watson, Phys. Rev. 156, 251 (1967).

PHYSICAL REVIEW B VOLUME 6, NUMBER 5 1 SEPTEMBER 1972

Mössbauer Study of Gold-Iron Alloys*

B. Window

Materials Physics Division (8), *Atomic Energy Research Establishment, Harwell, United Kingdom and Physics Department, Carnegie-Mellon University, Pittsburgh, Pennsylvania* 15213

(Received 29 November 1971)

Mössbauer results obtained at 300 and 4.2 K for Fe^{57} in alloys of 2–40 at.% iron in gold have been fitted with consistent values for the hyperfine interactions. The 300-K data are adequately fitted using a reducing-point-charge model based on a Thomas-Fermi-like model for the iron screening in gold, and the derived parameters are used in fitting the 4.2-K data. The sign of the electric field gradient is deduced to be negative, and information concerning the magnetic moment alignment with different numbers of neighbors is derived. The spins point along ⟨111⟩ crystallographic directions when the atom has two or more iron neighbors, and along directions normal to the iron-iron axis when it has one neighbor. With increased size of groups of atoms the spins point along the ⟨111⟩ axis that minimizes the number of Fe-Fe axes normal to it, until at about 16 at.% iron long-range ferromagnetism occurs due to the occurrence of linear chains. The results for higher-concentration alloys are consistent with those expected for a ferromagnetic random alloy.

I. INTRODUCTION

Gold-iron alloys have been studied using the Mössbauer technique with Fe^{57},[1–11] Sn^{119},[12,13] and Au^{197}[14] nuclei, and considerable information concerning the magnetic ordering has been obtained. However, in the case of Fe^{57} where complicated spectra are obtained above and below the ordering temperatures, a model which accounts for the spectra at both high and low temperatures and over a range of iron concentration has not been proposed. The Fe^{57} resonance shows distributions of isomer shifts, quadrupole splittings, and magnetic splittings, and while the analysis of the spectra is difficult because of these distributions, a careful interpretation can yield valuable information about the magnetic moment alignment with respect to the atomic neighbors. Also there has occurred in the